

Localization of plastic strain at the microstructural level in hastelloy X subjected to monotonic, fatigue, and creep loading: the role of grain boundaries and slip transmission

Wael Z. Abuzaid¹, Huseyin Sehitoglu² and John Lambros³

The localisation of plastic strain in polycrystalline metals is influenced by the microstructure. In this work, we study the localisation and heterogeneity of the plastic response using high resolution strain measurements via digital image correlation and microstructural characterisation using electron backscattering diffraction in monotonic tension, fatigue, and creep. We focus on the role of grain boundaries acting as barriers to dislocation motion. More specifically, we address slip transmission across grain boundaries and the importance of the residual Burgers vector in determining the cross-boundary reaction. We provide insight into how these cross-boundary reactions influence the accumulation of plastic strains across interfaces, dictate the locations of fatigue cracks, and affect the length of fatigue micro-cracks. The scope of the paper is partially a summary and overview of most recent published work as well as presenting new experimental results, particularly at elevated temperatures. The main outcomes of the agglomerate of experimental and analysis results are discussed with the intent to provide a deep understanding of the plastic response of the nickel-based superalloy, Hastelloy X, at different length scales and different loading and temperature conditions.

Keywords: Deformation heterogeneity, Digital image correlation, Microstructure, Grain boundaries, Slip transmission, Fatigue crack initiation, Grain cluster, Cyclic creep

Introduction

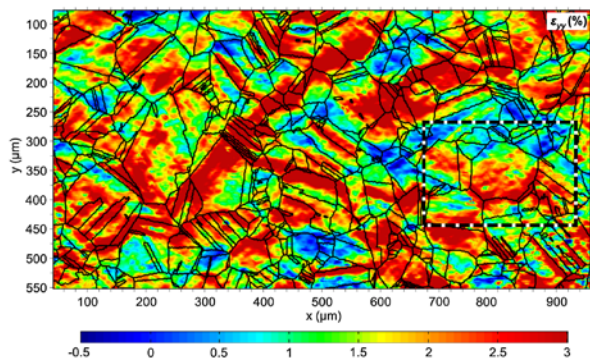
A quantitative understanding of localised plastic response at the micro-scale, i.e. grain and sub-grain level, is essential for the development of improved fatigue models with better predictive capability. At such scales, grain boundaries (GB) have a paramount role in introducing heterogeneity in the plastic response due to crystal anisotropy,¹⁻⁴ presence of defects in the GB plane,⁵ and by interacting differently with incident slip, i.e. dislocation moving within grains and interacting with GBs. This interaction can take the form of blockage, thus creating a pile-up and stress concentration,⁶⁻⁹ or slip transmission through the interface, either full or partial.¹⁰⁻¹³ In the case of transmission, and as will be shown in this work, high strains develop across the transmitting GBs and slip bands can extend across multiple grains, thus forming a grain cluster.¹⁴ The concept and importance of grain clusters have been discussed in the fatigue crack initiation literature.¹⁵⁻¹⁷ Blocking GBs, on the other hand, will shield certain grains/areas in the material resulting in low strain regions. These hard blocking GBs will not only impact where

plastic strain accumulates but can also act as crack initiation sites due to the stress concentration created by the impinging slip on the GB plane.¹³ This paper presents a wide range of experimental measurements and analysis in tension and fatigue, with sub-grain level resolution, and aims to improve our predictive capability of GB response (i.e. transmitting or blocking).

The basic understanding of slip transmission has primarily evolved through significant experimental work utilising the TEM.^{10,18} Different GB/dislocation types were considered and through extensive analysis, predictive criteria for the cross-boundary reactions were proposed.^{10,11,18,19} More recently, further insight has been made possible through atomistic simulations (molecular dynamics).²⁰⁻²⁴ The previous efforts have been focused on proposing and refining our predictive capability of slip transmission (i.e. if the incident slip and GB type are known, which slip system will be activated in the neighbouring grain and how will the GB be modified). There has been less effort, however, on studying the impact slip transmission has on a larger scale in the form of how it influences plastic strain accumulation and heterogeneity of deformation at the microstructural level. The work presented in this paper has focused on this aspect and makes quantitative assessment of the importance of the residual Burgers vector in determining the GB resistance to transmission and strain

¹Department of Mechanical Engineering, American University of Sharjah, PO Box 26666, Sharjah, UAE, ²Department of Mechanical Science and Engineering, University of Illinois at Urbana-Champaign, 1206 W. Green St., Urbana, IL 61801, USA, ³Department of Aerospace Engineering, University of Illinois at Urbana-Champaign, 104 S. Wright St., Urbana, IL 61801, USA

*Corresponding author, email huseyin@illinois.edu



1 Contour plot of the vertical (ϵ_{yy}) strain field (along the loading direction) with overlaid grain boundaries. A significant level of deformation heterogeneity can be observed from the contour plot. Adapted from Figure 3 in ¹⁴.

accumulation across the interface (the residual Burgers vector b_r is one of the key factors controlling the transmission reaction as proposed by Lee *et al.*,^{10,18} the criterion is referred to as the LRB criterion for slip transmission thereafter). The conclusions are made through the consideration of polycrystalline specimens consisting of hundreds of grains, thus assuring statistical relevance.

AQ4 Fatigue micro-crack formation is also a focus in this work. Despite extensive work, both experimental and modelling, fatigue remains one of the major sources of failure.^{25–28} The complexity of a problem like fatigue makes developing a comprehensive model which spans across all the relevant length scales, accounts for microstructural features of importance, and considers material defects or strengthening elements a non-trivial task. On the experimental side, the wealth of the experimental work has been focused on total life where macroscopic material response (i.e. stress or strain) measurement is made, qualitative microstructural analysis of crack initiation sites, high resolution TEM observations of dislocation structure arrangements due to cyclic loadings, and fatigue crack growth.²⁹ To a lesser extent, full-field strain measurements have been used to monitor strain evolution under cyclic loading conditions.^{30–32} It is widely accepted, however, that localised plasticity is a precursor and necessary condition for the nucleation of cracks.^{27,28,33–36} Full-field strain measurements depicting the development of plastic strain within individual grains in a polycrystalline material subjected to fatigue loading can help map out the ‘hot spots’ for crack nucleation. In this context, GBs are of particular interest as they can act as crack nucleation sites. An aspect that deserves more quantitative assessment is how the GB resistance to slip transfer can influence the development of critical cracks from nucleation to micro-crack propagation (crack formations) and eventually reaching a critical length. The results reviewed in this paper show an experimental and analysis procedure that provides quantitative information and a clear connection to micro-crack formation (nucleation and micro-crack propagation). The development of local plastic heterogeneity and the GB resistance to slip transmission, in terms of residual Burgers vector, are discussed as they impact/control the hot spots for fatigue crack initiation. Given the quantitative nature of the results, the conclusions can aid the refinement of fatigue crack initiation models and the development of an improved crack initiation criterion.

The nickel-based superalloy Hastelloy X has been primarily used in high temperature applications, such as in turbine engine components. In general, the majority of the available experimental work at elevated temperatures has been focused on simple loading conditions, such as tension

or compression,^{37–39} isothermal fatigue,^{40–42} fatigue crack growth,^{43–47} creep,^{48,49} and dynamic response at different temperatures.⁵⁰ There has been less effort considering more complex thermo-mechanical loading conditions involving temperature cycling.^{48,51} Also, despite the fact that there are a few studies involving full-field measurements of strain,^{39,43} most of the available work reports average measurements at the macro-scale (e.g. creep strain rate). Material models under such creep conditions rely on these average measurements of creep strain rate. To the best of our knowledge, there is no experimental data available showing how much the local creep strain rate differs from the commonly reported average measurements. The last part of this work extends some of the analysis and experimental procedures developed at room temperature to investigate Hastelloy X at elevated temperatures.

In summary, this paper reviews some recent experimental work by the authors on the high temperature nickel-based superalloy Hastelloy X. Unique experimental and analysis methodologies are presented which provide a quantitative assessment of heterogeneity developing within individual grains and in the vicinity of GBs. A correlation between GB resistance to slip transmission and the accumulation of strains across the interface is discussed in terms of inducing heterogeneity in the deformation and influencing the hot spots for the formation of critical fatigue cracks. Lastly, some insight into the high-temperature performance is provided with full-field quantitative measurements of the localisation and accumulation of creep strain in ratcheting creep deformation mode.

Materials and methods

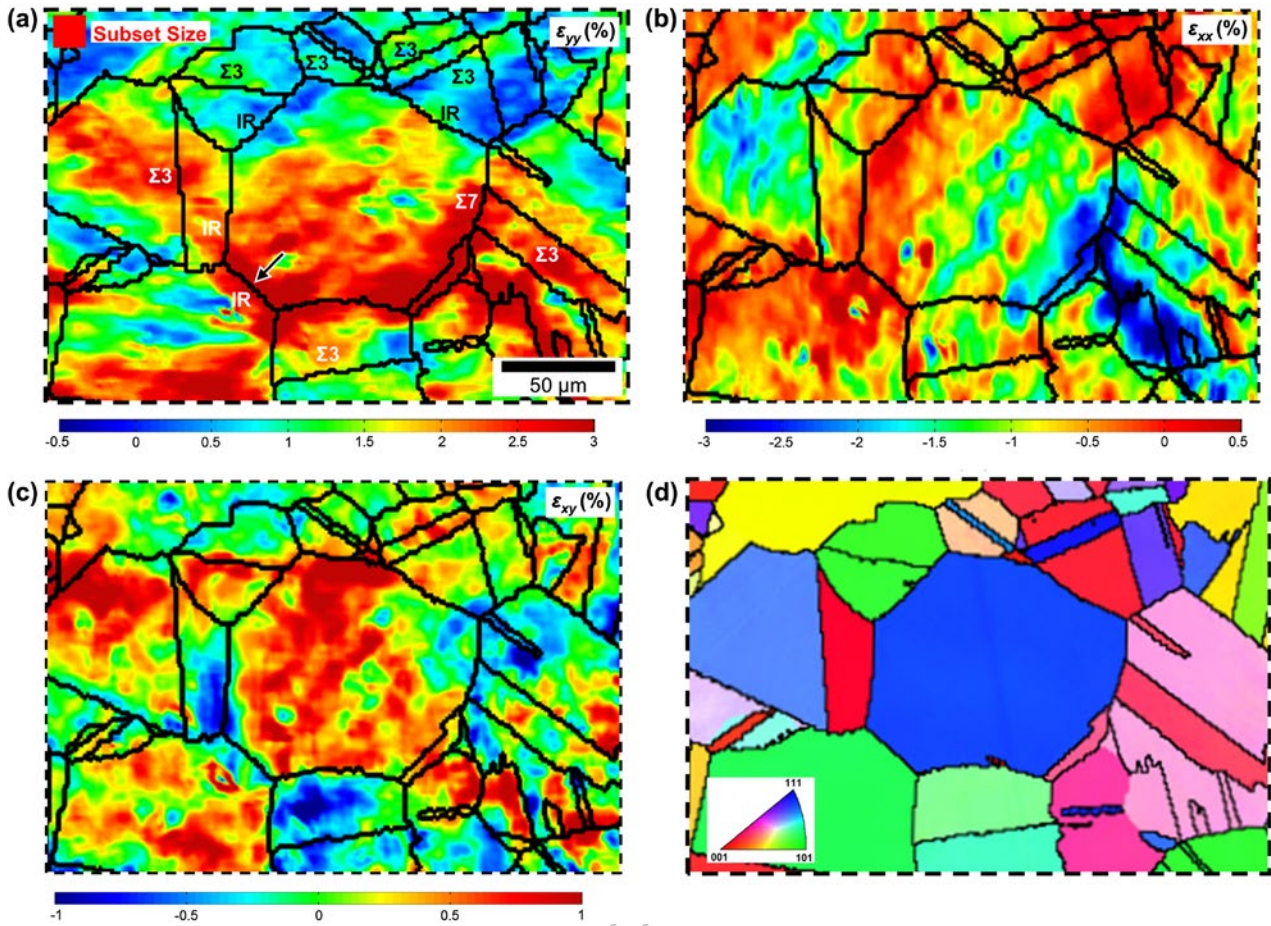
Material and experimental details for the monotonic tension results have been presented in¹⁴ and for the fatigue results in⁵². For the cyclic creep experiment, and in order to allow for DIC measurements at elevated temperatures (up to 650 °C), the surface (i.e. DIC region of interest) was painted with high temperature white paint and then speckled with high temperature black paint (using an airbrush). Adding a layer of paint on the surface helped reduce surface changes due to oxidation, thus enabling DIC measurements. Throughout the experiment, the stress was held constant while the temperature was cycled. An induction heater was used to achieve the desired sample temperature which was measured on the back surface of the sample using a thermocouple. The details of the loading conditions are summarised below.

- (1) In the load frame and at zero stress, the sample was heated from room temperature to 450 °C.
- (2) After initial heating, the sample was loaded to 306 MPa, 25% more than the yield stress at 650 °C, which was maintained throughout the experiment.
- (3) After applying the mechanical load, the temperature was cycled between 450 and 650 °C using a temperature controller. The cycle time was set to 4 min, the fastest allowable by the induction heater controller.
- (4) Images of the region of interest were captured *in situ* during the test.

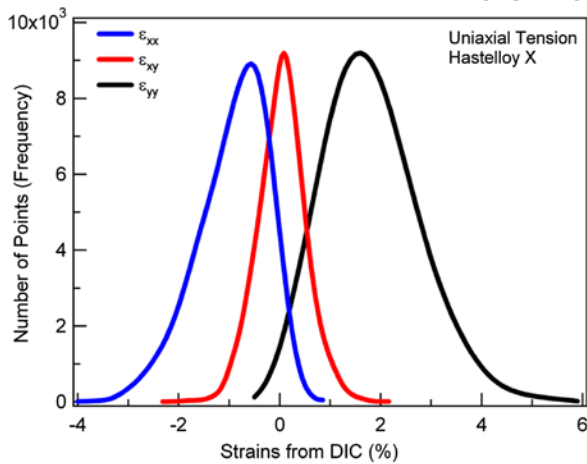
Results and analysis

High resolution strain measurements with sub-grain level resolution

A dog bone specimen was deformed in uniaxial tension to a total residual plastic strain of ~2% nominal strain. Prior to loading, a region on the sample’s surface was characterised using EBSD for microstructural information



2 a Enlarged view of the region outlined with the black rectangle in Figure 1. b–c Contour plots of the horizontal strain field ϵ_{xx} and the shear strain field ϵ_{xy} in the same region shown in a, respectively. The grain orientation map from EBSD is shown in d. Reproduced from Figures 1 and 3 in ¹⁴.



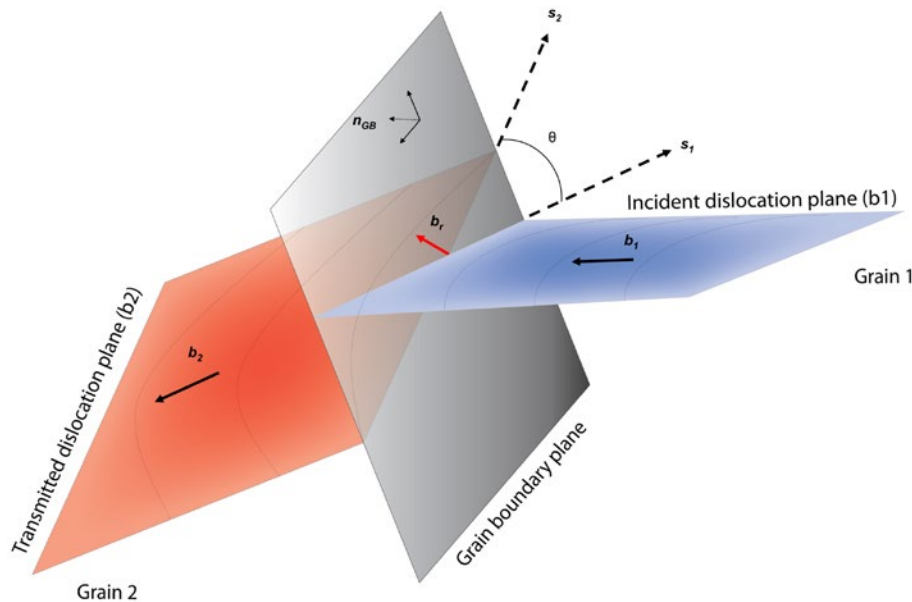
3 a Strain histograms of the horizontal (ϵ_{xx}), shear (ϵ_{xy}), and vertical (ϵ_{yy}) DIC strain fields. For the strains in the loading direction (ϵ_{yy}), the mean strain matches the applied strain but the range of magnitudes spans between ~ -0.5 and 6%. The width of the histograms in Figure 3 indicates heterogeneity in the local strain fields.

and high-resolution reference images for DIC strain measurements were captured using an optical microscope. After loading and unloading the sample, deformed images of the same regions were captured for DIC measurements

(full details of the experimental set-up and DIC details can be found in¹⁴). Figure 1 shows the contour plot of the vertical strain field (ϵ_{yy} , along the loading direction) for the entire region of interest. A reduced region is enlarged and shown in Figure 2 along with the other measured strain components, the horizontal strain field ϵ_{xx} and the shear strain field ϵ_{xy} . As EBSD orientation characterisation was made in the same DIC region, grain orientation and GB locations are known and were overlaid on top of the DIC strain contour plots. As in any surface measurement technique, full characterisation of the strain tensor is not possible; the shear strain components in the third direction, ϵ_{xz} and ϵ_{yz} remain unknown. The vertical strain in the third direction, however, can be calculated by assuming plastic incompressibility through the following equation:

$$\epsilon_{zz} = -1 \times (\epsilon_{xx} + \epsilon_{yy}) \quad (1)$$

The previous figures provide clear visual evidence of a high level of deformation heterogeneity within individual grains. An alternate way to view the results, which provides quantitative means for assessment of the level of deformation heterogeneity, is to construct strain histograms from the measured DIC contour plots. Figure 3 shows strain histograms for the three measured strain components in the entire field. A wide distribution of strain magnitudes (-0.5 to 6%) is seen in the ϵ_{yy} strain histogram. Although the mean strain (averaged from DIC full field or the strain histogram) matches the nominal residual strain measured using an extensometer, the high strain regions were three times higher compared



4 Schematic of slip transmission through a grain boundary, where b_1 and b_2 are the Burgers vector of the incident and transmitted dislocations across the GB plane, respectively. θ is the angle between the lines of intersection between slip planes of the incident and transmitted dislocations and the GB plane. b_r is the residual dislocation left in the GB plane due to slip transmission. Adapted from Figure 10 in ¹⁴.

AQ10

to the nominal strain. Similar observations can be deduced from the strain histograms constructed for the other two strain components.

Slip transmission across grain boundaries

As slip interacts with GBs in a plastically deforming polycrystalline metal, one of the outcomes of this interaction is slip transmission across the GB. If full transmission takes place, the process is completed leaving no residual dislocation in the GB plane (i.e. cross slip). However, in many cases, this cross-boundary reaction takes place while leaving a residual dislocation (the residual Burgers vector b_r). If the Burgers vector of the incident and transmitted slip is known (b_1 and b_2 , respectively), then b_r can be calculated using the following dislocation reaction equation:⁵

$$\vec{b}_r = \vec{b}_1 - \vec{b}_2 \quad (2)$$

In the classical experimental work on slip transmission, the Burgers vectors were determined using the TEM, while in simulation work, they were determined from MD simulations. In this work, and as the scope was to investigate hundreds of GBs in a polycrystalline metal, we approximate the calculation of b_r using magnitudes of the slip direction (l_1 and l_2) of the incident and transmitted slip (see schematic in Figure 4).⁵³

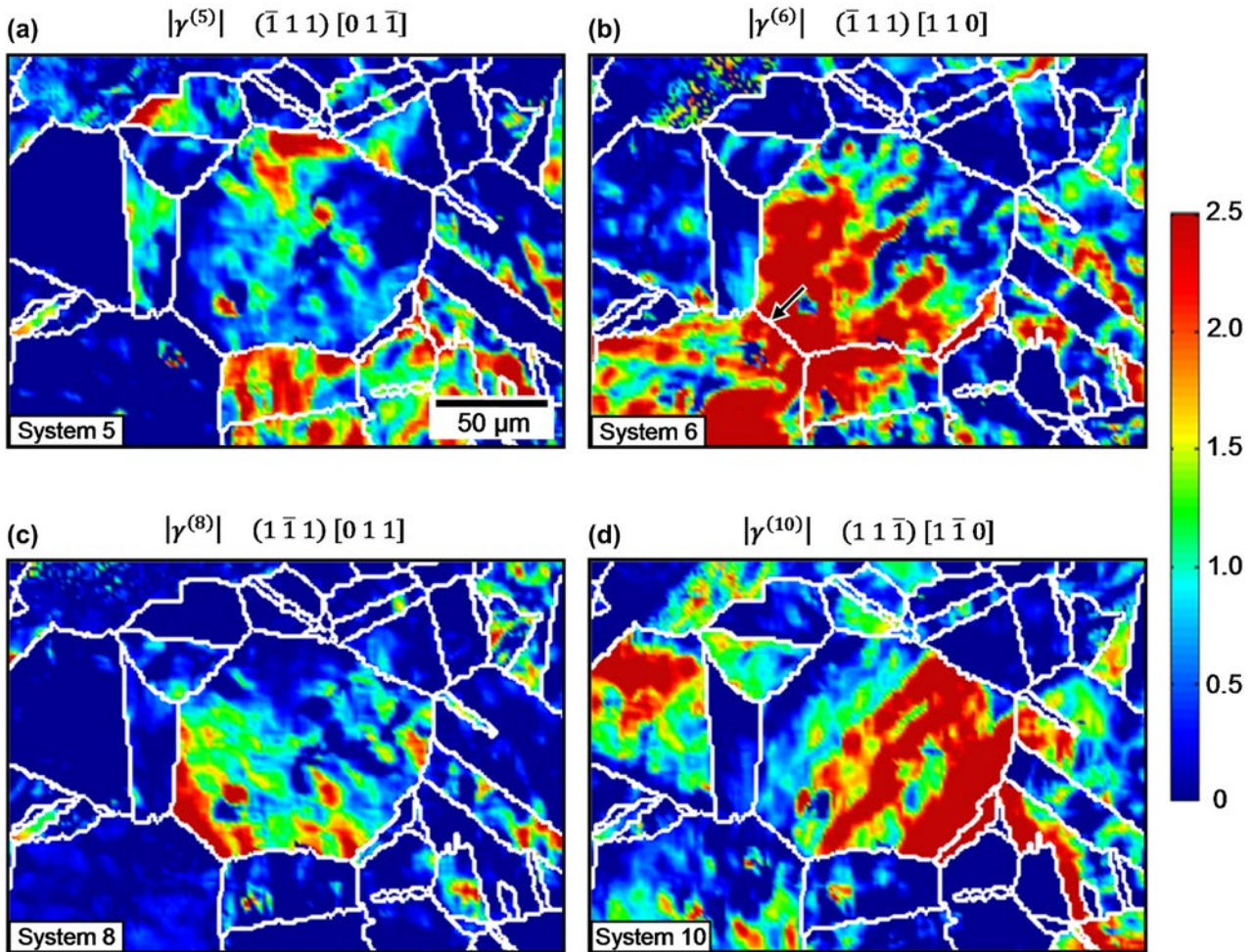
$$|\vec{b}_r| = l_1 - l_2 \quad (3)$$

For utilisation of Equation 3, the activated slip systems across each of the transmitting GBs in the entire microstructure have to be determined. We address this aspect by finding the local shear increments $d\gamma^\alpha$ for the 12 FCC slip systems, locally, across the entire microstructure. Plastic strain in the case of slip is achieved through these shear increments in the activated slip systems.⁵⁴ The following equation shows the relation between plastic strain and the shear increments:

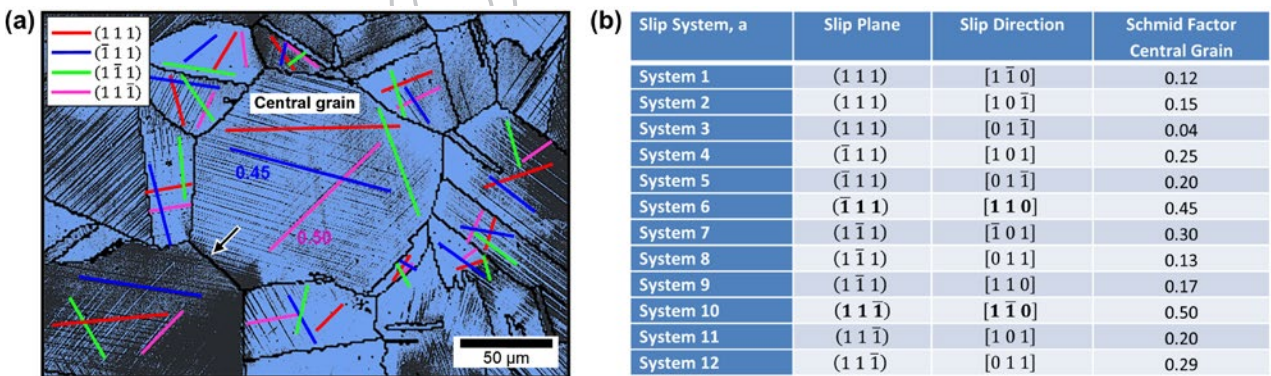
$$d\varepsilon_{ij}^p = \frac{1}{2} \sum_{\alpha=1}^s (n_i^\alpha l_j^\alpha + n_j^\alpha l_i^\alpha) d\gamma^\alpha = \sum_{\alpha=1}^s (m_{ij}^\alpha) d\gamma^\alpha \quad (4)$$

where α is the slip system number (one of the 12 FCC slip systems), S is the number of slip systems (12 for FCC), n^α is the vector defining the normal to slip plane for system α , and l^α is the vector defining the slip direction (both are known for FCC crystals). Three components of the plastic strain tensor were measured from DIC (ε_{xx} , ε_{yy} , ε_{xy}). The fourth component, ε_{zz} , was calculated by assuming plastic incompressibility. With the high resolution DIC strain measurements along with orientation information from EBSD, a viscoplastic constitutive model was used to solve for the shear strain increments spatially across the entire microstructure (see ¹⁴ for additional details on the procedure). Knowing the activated slip systems across transmitting GBs (note that these are the $\{111\}$ and $\langle 110 \rangle$) gives sufficient information to find b_r using Equation 3 (the orientation data allow writing both slip directions, incident and transmitted in crystal frame and direct utilisation of Equation 3). The strain contour plots in Figure 5 show an example of the shear increments for the same region shown in Figure 2 (only 4 out of the 12 are shown, the ones with the highest magnitudes). The activated slip systems' results are in agreement with slip trace and Schmid factor analysis as shown for a particular grain in Figure 6.

Figure 2 shows examples of GBs where clear strain accumulations were detected across the interfaces. Focusing on a particular GB (marked in Figure 2a), the SEM micrograph in Figure 7 shows clear slip traces across the GB which we associate with slip transmission across the GB. With the activated slip systems known (see Figure 5 for shear increments in the region containing the GB of interest), the residual Burgers vector was calculated using Equation 3 for the observed active slip systems across the GB. The results are shown in Figure 8 (inset to the left of Figure 8). Also shown in the figure is a parameter representing the Schmid factors for the incident and transmitted slip systems considered in calculating b_r (the term GB Schmid factor is used). Another case is also shown in the figure (inset to the right of Figure 8) representing the same incident slip but transmission to a different slip system across the GB (can think of this as a hypothetical case, no clear activation of the



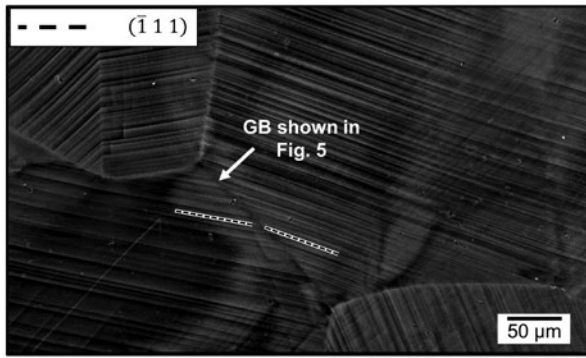
5 a–d Contour plot of the crystallographic shear increments for the region shown in Figure 2. Only the highest four activated systems are shown for increased clarity (systems 5, 6, 8, and 10). Different slip system activity in different regions of the central grain is clearly seen. Some systems are only activated in the vicinity of some grain boundaries (e.g. systems 5 and 8). Adapted from Figure 9 in ¹⁴.



6 SEM micrograph of the same region shown in Figure 5. Slip trace analysis shows activation of slip systems 6 and 10 in the central grain. The activated plane was determined using the EBSD orientation data (plot the traces of the {111} planes) and the final determination of the actual system was based on Schmid factor analysis as shown in b. The results are in agreement with the shear increment analysis shown in Figure 5. Adapted from Figure 7 and Table 1 in ¹⁴.

70 plotted slip system across the GB was observed indicating no transmission). The GB Schmid factors for both of these cases are similar; however, the magnitudes of b_r are different. The hypothetical case shown in the inset to the right would produce a high residual Burgers vector compared to the other case where we believe transmission actually took place. The analysis from this case not only provides support to the LRB

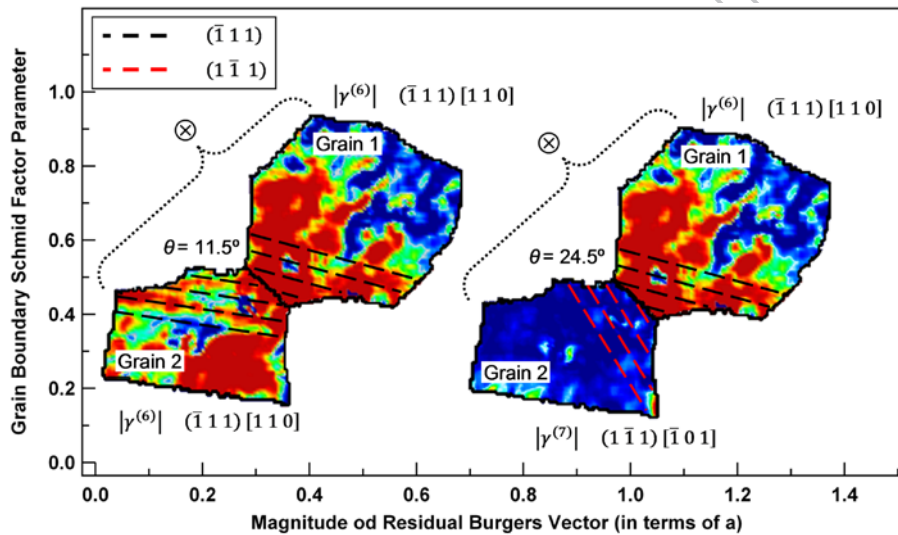
10 criterion that minimising b_r is a very important condition in determining the cross-boundary reaction but also suggests a correlation between slip transmission and the magnitudes of strain across GBs that develop during plastic deformation. Figure 9 presents an additional example which shows a special case of a twin boundary and cross slip across the interface.



7 SEM micrograph of the deformed sample showing traces of the activated slip systems in the vicinity of the GB shown in Figure 5 (marked with arrow in Figure 5b). Continuous slip traces across the GB were observed and the corresponding slip planes were the $(\bar{1}11)$ slip planes (system 6 is on the (111) slip plane). These observations are consistent with the analysis made using shear strain calculations as shown in Figure 6.

results presented in Figure 11 show the loading conditions and vertical strain field ϵ_{yy} for each of the deformed states. The results show clear cases of the formation of grain clusters or groups of connected grains with high strain magnitudes. Also shown are low strain regions that show minimal contribution to the total measured strains. Shielding GBs that are not conducive to the transmission of slip are expected to be a key contributor to the formation of these low strain regions (a few shielding GBs are marked in Figure 11). The observations of formation of grain clusters and shielded regions with low strains seem to hold as loading is incrementally increased.

Figure 12a shows strain histograms constructed from all the measured deformed states. In addition to the expected increase of the mean strain after each loading increment, the histograms also widen – a clear indication of an increased level of deformation heterogeneity developing in the material with loading. To better interpret this increase in the level of heterogeneity, the evolution of the minimum and maximum strains (from the full-field DIC) was plotted in Figure 12b. Also we plot a strain field obtained by subtracting the Def.4



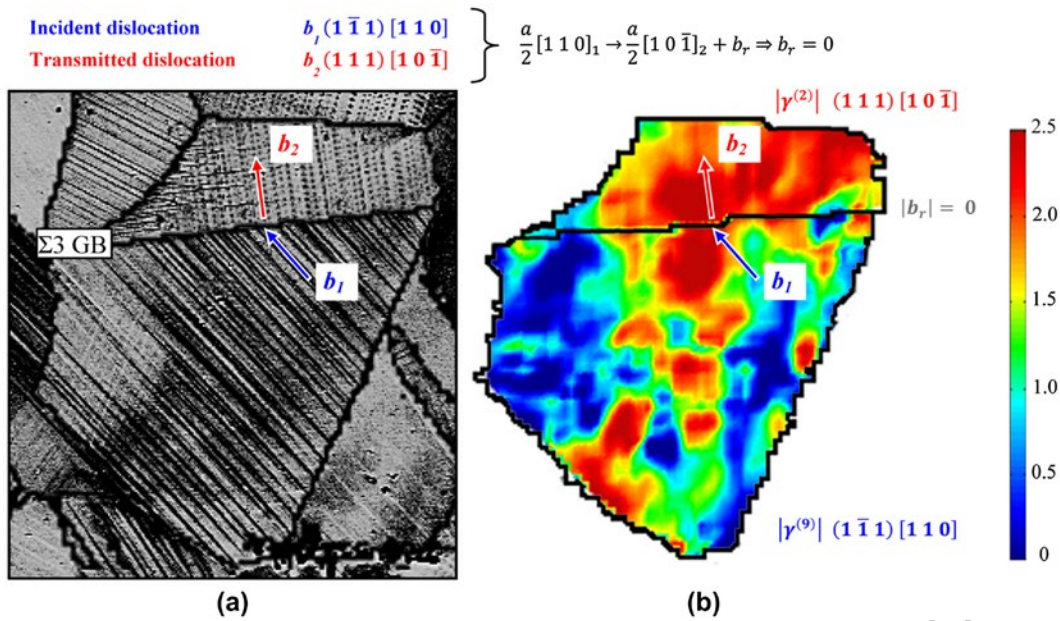
8 Grain boundary Schmid factor parameter vs. the magnitude of b_r . The point to the left represents the interaction between slip system 6 in grain 1 and system 6 in grain 2. The contour plots of the shear increments show activation of systems 6 in mantle regions across the GB (associated with slip transmission). The point to the right represents the interaction between systems 6 and 7. No transmission from system 6 in grain 1 to system 7 in grain 2. Notice the high residual Burgers vector associated with this possible interaction. Adapted from Figure 11 in ¹⁴.

state from the Def.5 state (shown in Figure 13), thus giving the active regions of strain accumulation between Def.4 and Def.5. From these two plots (i.e. the strain histograms and the Def.5-Def.4 contour plot), we see that the magnitude of strain in high strain regions (i.e. spatial regions in the DIC field having the highest measured strain) increases at a much faster rate compared to the mean strain and that the minimum strain remains almost unchanged. This contour plot explains the previous observations by clearly showing that the same regions of strain accumulation after Def.2 continued to be active and accommodate plasticity at Def.5. In other words, the formation of grain clusters and shielded regions of low strain were observed early and at low levels of plastic strain (Def.2). This continued accumulation of strain in the same spatial regions and the lack of relative activity in other regions have resulted in this increased level of heterogeneity in the plastic response.

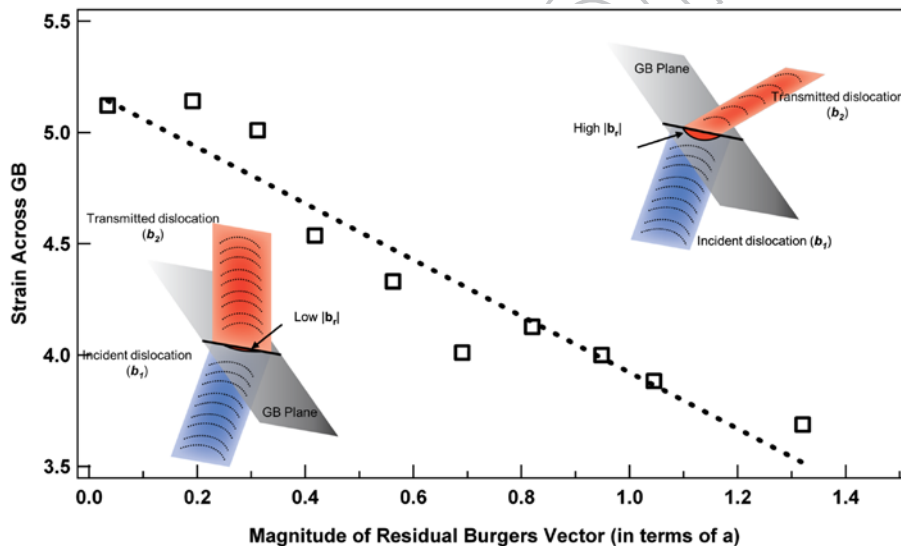
To assess the importance of the case analysed Figure 8 from a statistical perspective, we interrogate the entire microstructure by making similar calculations for each and every GB. The GBs were binned based on the magnitude of b_r . For each bin, the average strain across GBs was calculated. The results of this analysis are shown in Figure 10. The figure clearly shows an inverse relation between strain accumulation and the magnitude of b_r .

Strain evolution in uniaxial tension – deformation heterogeneity

The focus of this part is on quantifying the evolution of deformation heterogeneity. This is achieved by measuring the accumulation of plastic strains (high resolution along with EBSD characterisation of the microstructure) in a sample subjected to incremental monotonic loading. The



9 Slip transmission through a $\Sigma 3$ GB. *a* SEM micrograph showing continuity of slip traces across the GB. The shear strains associated with the observed traces are shown in *b*. The directions and magnitudes of both systems across the interface indicate slip transmission through the GB with $|b_r| = 0$ (*a* represents the lattice spacing of the material). Adapted from Figure 4 in ⁶².

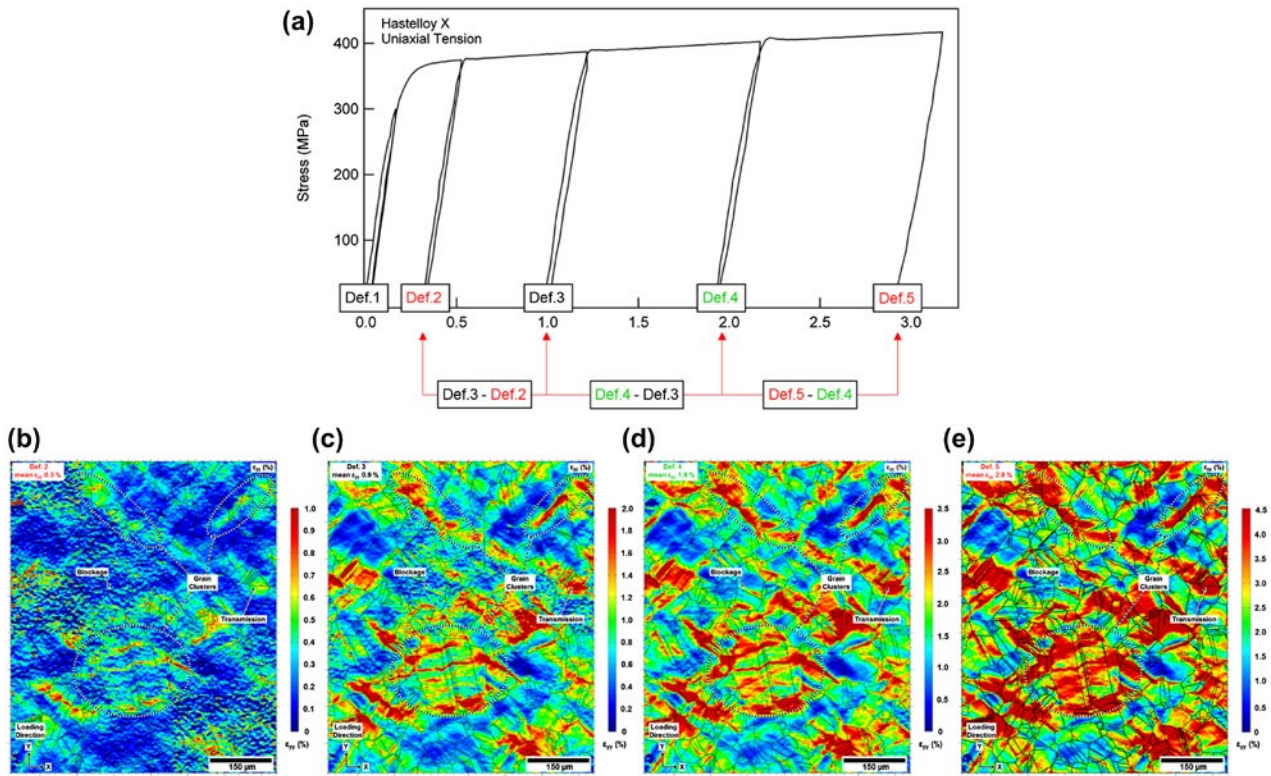


10 Strain across grain boundaries vs. b_r . The strain across GBs is calculated by adding the average strains in both mantles (i.e. GB regions) across the boundary. Boundaries that show higher strains across the GB exhibit lower magnitudes of b_r . This can be related to the GB resistance to slip transmission. Adapted from Figure 13 in ¹⁴.

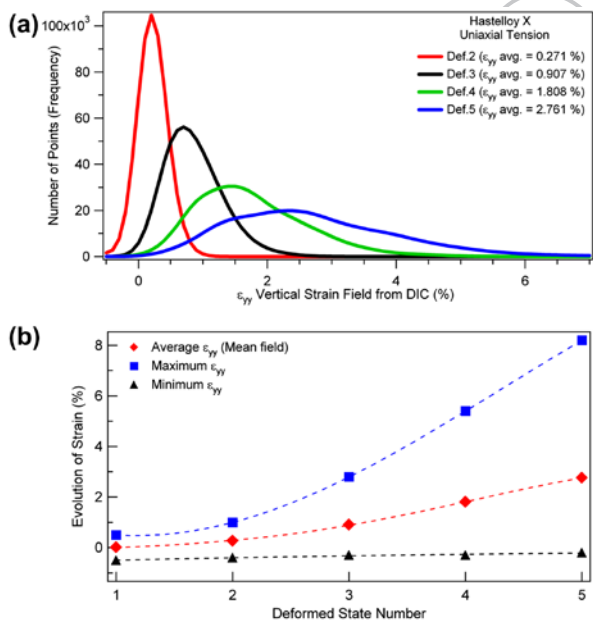
Fatigue crack formation

5 Cyclic strain localisation is a precursor to the nucleation of fatigue cracks.^{13,27,28} This part of the work is focused on studying fatigue crack initiation resulting from strain heterogeneities at the microstructural level and in the vicinity of grain boundaries. The same experimental and analysis procedures discussed previously were used to shed quantitative insight into the formation of fatigue cracks in Hastelloy X. The full experimental details can be found in⁵²; in this section, we only highlight the main outcomes. Figure 14 shows the hourglass specimen with highlighted microstructure of the region on interest. The sample was loaded in stress control with -1 R ratio (fully reversed) and

the stress level was 900 MPa as shown in Figure 14c. High resolution DIC measurements were made at Point A during the loading (Figure 14c) which was after 1,000 fatigue cycles. No fatigue cracks were observed at that point in the fatigue life, note that the images for DIC were captured using the optical microscope at 25 \times magnification. The sample was then loaded for an additional 9,000 cycles, to Point B in Figure 14c. Clear fatigue cracks were observed in the optical microscope at that stage of the loading. An additional half cycle was applied to further open the cracks for better visualisation, Point C in Figure 14c. Figure 15 shows a selected region with optical images of the reference state prior to loading, at loading Point A (1,000 fatigue cycles and no visible fatigue cracks), at loading Point B (after 10,000 cycles and obvious



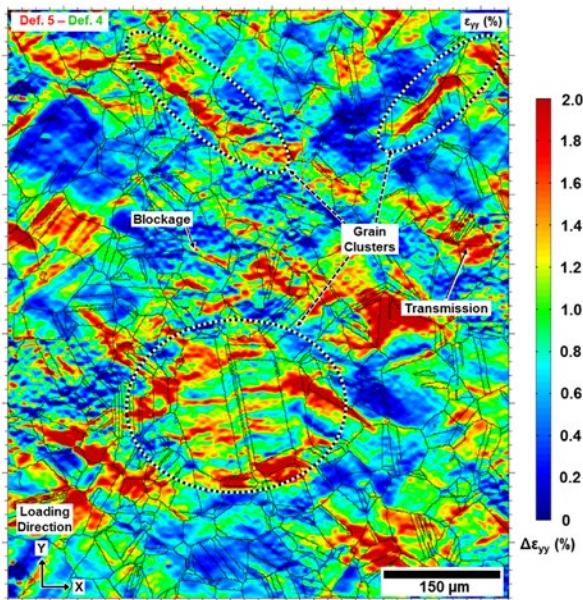
11 a Stress-strain curves showing the loading history for the uniaxial tension sample. The reported strains are from DIC average fields. *Ex situ* DIC was performed at the end of each loading cycle (Def.1, Def.2, Def.3, Def.4, and Def.5). *b-d* Contour plots of the vertical (ϵ_{yy}) strain fields with overlaid grain boundaries for all deformed states. Notice the strain accumulation in the vicinity of some GBs in *b* and the early signs of shielding and slip transmission, which leads to the formation of grain clusters. These observations (i.e. formation of grain clusters, slip transmission, and shielding) at low magnitudes of plastic strain seem to hold with continued loading (compare the marked regions in *b-d*).



12 a Strain histograms of the vertical (ϵ_{yy}) strains for all deformed states shown in Figure 11a. The maximum strain (i.e. the right end of each histogram) increases more than the increase in the minimum strain (i.e. the left end of each histogram). *b* Evolution of the minimum, mean, and maximum field strains. Maximum strains increase significantly while minimum strains make minor change. The figures indicate that the level of deformation heterogeneity increases with additional accumulation of plastic strains.

fatigue cracks), and an SEM micrograph at Point C (10,000 cycles + 1/2 tension cycle to open up cracks).

Figure 16a shows the vertical strain field along the loading direction ϵ_{yy} along with the GB locations from EBSD. Although the field average was 0.58% only, high strains up to 2% were measured. All of the reported strains were measured before the observation of the fatigue cracks. Utilising this early measurement of strain in the fatigue life of the sample, we focus our analysis on understanding the correlation between the locations where fatigue cracks eventually form and the initial accumulation of plastic strain prior to the formation of these cracks. This can be assessed visually by overlaying the strain contour plot (taken at 1,000 cycles, no cracks) onto the optical images showing micro-cracks after 10,000 fatigue cycles (so the contour plot and the optical images showing cracks are not at the same number of cycles). This plot is presented in Figure 16b and shows an obvious correlation between the locations of the observed fatigue cracks and the prior strain localisation. Also, the figure suggests that the length of high strain regions (which may form due to the presence of GBs allowing slip transmission) controls the length of the observed fatigue cracks. An enlarged region is shown in Figure 17a, the length of the measured localised slip extending across multiple grains (grain cluster) compares to measured crack lengths observed in the same region 9,000 cycles after making the strain measurements (Figure 17b). Similar measurements were made for all the observed fatigue cracks across the entire microstructure in the region of interest. The results are shown in Figure 17c-d and provide further evidence supporting the presence of a strong

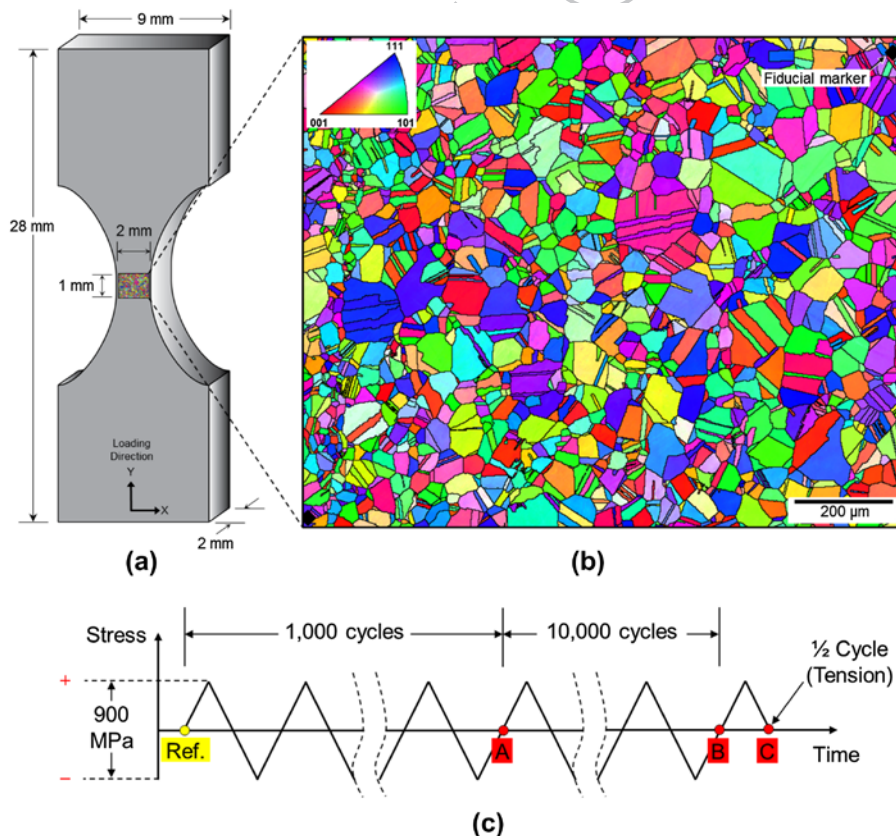


13 Strain contour plots (ϵ_{yy}) of the difference between two deformed states, Def. 5 and Def. 4. The contour plot was generated by subtracting the contour plot shown in Figure 11d (Def. 4) from the contour plot in Figure 11e (Def. 3), thus enabling the determination of the active regions of strain accumulation between Def. 4 and Def. 5. The contour plots indicate that the strain evolution with additional loading cycles takes place in relatively the same regions.

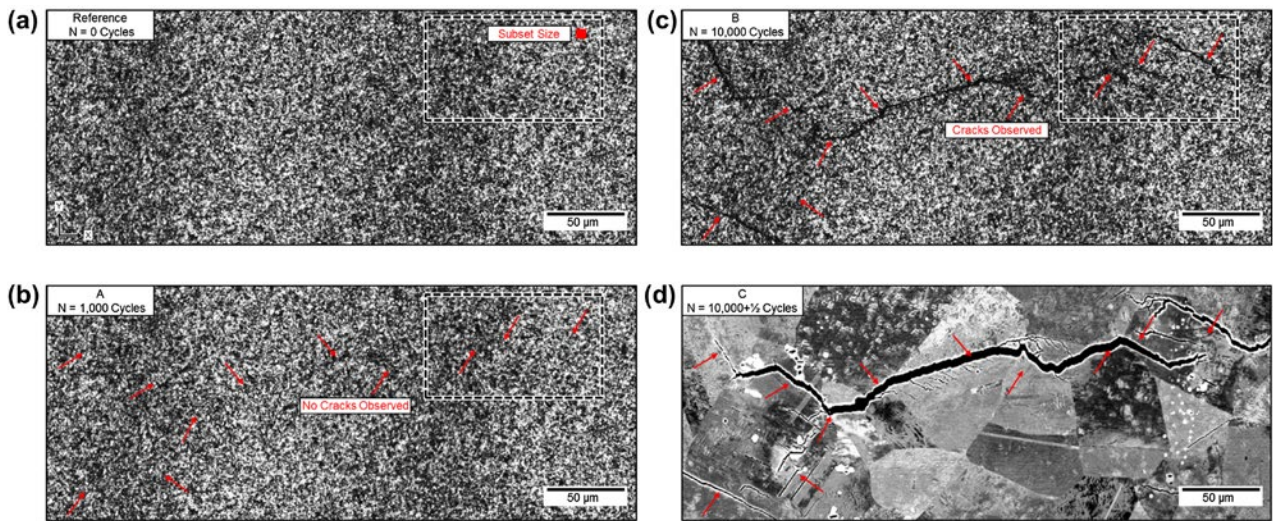
correlation between the crack formation lengths (initiation and micro-crack propagation) and the length of the localized slip bands which form earlier in the fatigue life.

As discussed previously, GBs play an important role in inducing deformation heterogeneity and can either shield certain regions by blocking slip or assist in the formation of grain clusters by allowing transmission across the interface into neighbouring grains. We focus our analysis now on how these differences in GB response influence the observed fatigue cracks. Figure 18 shows an example of a shielding GB where high strains were measured on one side of the GB. The fatigue cracks associated with this case were limited in length and confined within the grain which showed earlier slip activity. The residual Burgers vector that would have been produced in case slip transmission took place can be calculated for this case by determining the activated slip system in the grain showing strain accumulation and by considering the slip directions of the slip systems with the highest Schmid factors across the interface. The results are shown in the table at the bottom of Figure 18. We note that the magnitudes of b_r are rather high and that could explain why transmission never happened in the first place. There are potentially other factors affecting why transmission did not take place, such as low Schmid factor, but the final outcome is that shielding was observed and that led to fatigue cracks being confined into one of the grains across the interface.

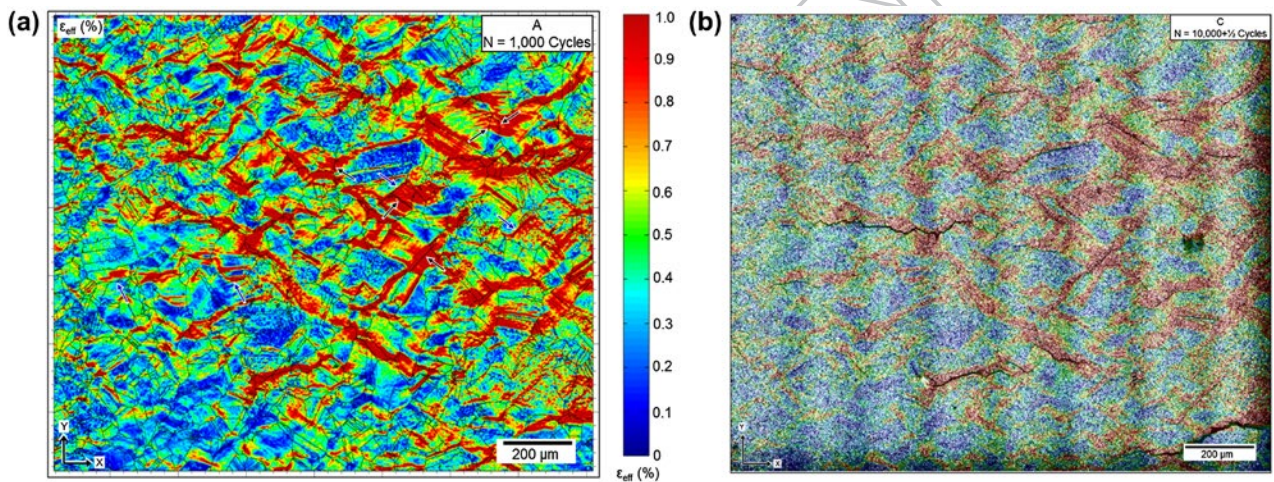
Figure 19 shows a similar analysis but where a transmitting GB was considered. Strains were measured across the interface (Figure 19a) and the resulting fatigue



14 a Schematic showing the fatigue sample dimensions. The entire reduced cross section was considered in EBSD, DIC, and SEM analysis. b Grain orientation map of the region of interest from EBSD. c The fatigue loading history and the number of cycles at which DIC measurements and crack observations were made. Reference images for DIC were captured prior to loading. After 1,000 fatigue cycles, the sample was unloaded and removed from the load frame to capture deformed images covering the entire gauge area (state marked 'A'). After 9,000 additional loading cycles, point 'B', fatigue cracks were observed. The half cycle leading to point 'C' was applied to open the micro-cracks for better visualisation. Adapted from Figures 2 and 3 in ⁵².



15 a An example of a selected region imaged before loading (reference images for DIC). b The same region but at deformed state 'A' (i.e. after 1,000 fatigue loading cycles). No visible cracks were observed at this state. The red arrows point to regions in which cracks were detected at deformed state 'B' (i.e. after 10,000 fatigue loading cycles) as shown c. For better visualisation of the initiated micro-cracks, the sample was subjected to a half cycle (state 'C', tensile portion only) to open the cracks, and images were taken in the SEM as shown d. Adapted from Figure 4 in ⁵².



16 a Contour plot of the effective plastic strain field () across the entire region of interest. Some of the strain localisations are concentrated around GBs (examples are marked with blue and white arrows) and others extend through multiple GBs (examples are marked with black and white arrows). b Overly of plastic strains shown in a onto the deformed images at state 'C' (10,000 + 1/2 Cycles). Micro-cracks of varying lengths are distributed across the entire gauge area. A strong correlation between strain localisation and the locations and lengths of the observed cracks is clear from the figure. Adapted from Figures 7 and 8 in ⁵².

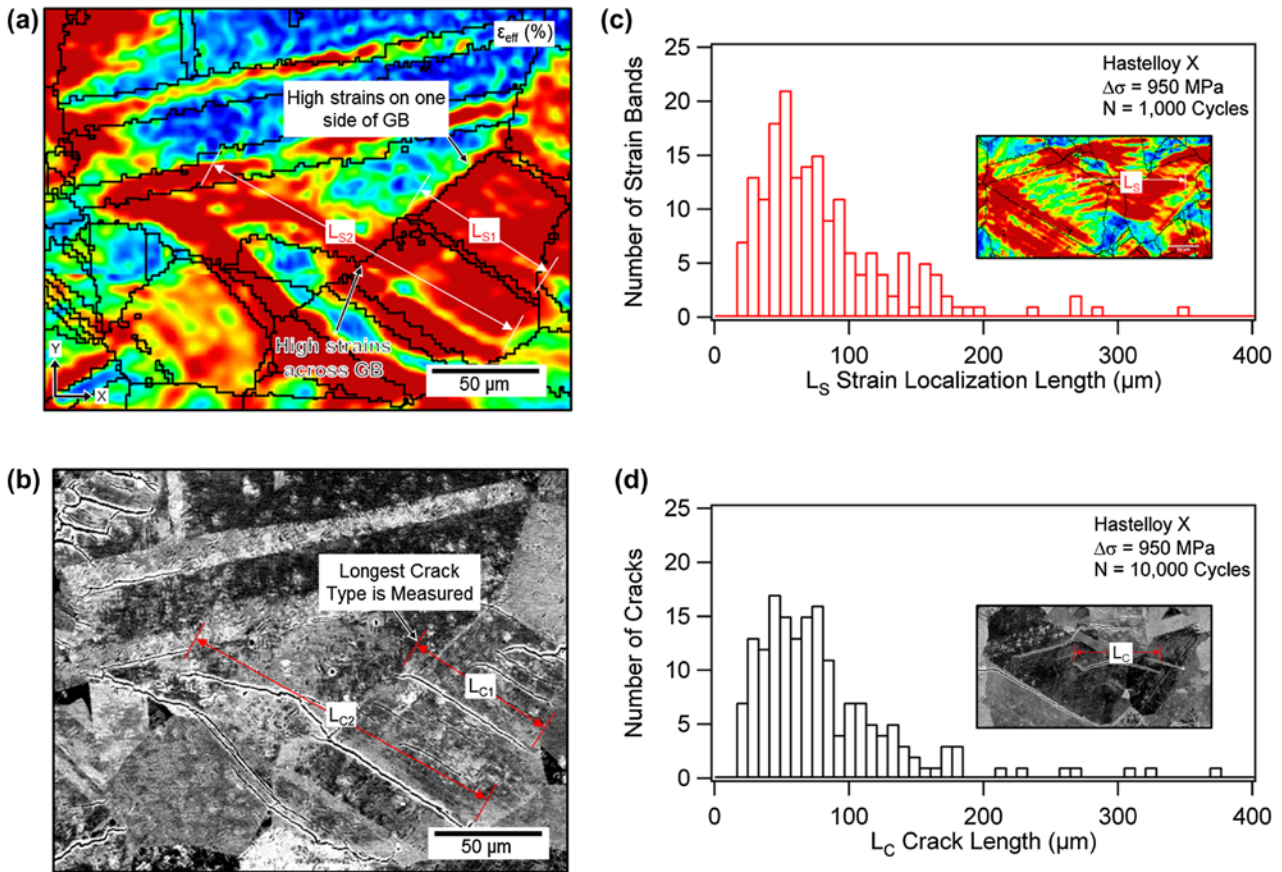
cracks extended transgranularly through the GB and followed the length of the transmitted slip (i.e. crack along the grain cluster as shown in Figure 19b). The analysis of the local slip system activity (Figure 19c) and the calculation on b_r for the sequence of transmission across the two shown GBs indicate low magnitudes of b_r (0.5 and 0 as shown in the table at the bottom of Figure 19) compared to the shielding case discussed previously. As these GBs were conducive to slip transmission, longer slip localisation lengths compared to the shielding case were measured and the resulting fatigue crack was relatively long (~100 μm, average grain diameter is ~24 μm).

Cyclic creep

This part of the work aims to investigate the localisation and evolution of creep strain (plastic strain) at elevated temperatures. The loading conditions are shown in Figure 20

and the evolution of the ϵ_{yy} vertical strain versus time is shown in Figure 21 (DIC field averages). Only selected temperature cycles are shown in the figure along with the initial loading cycles (thermal and mechanical). Yielding took place during the initial mechanical load and as the selected stress level was 1.25 times the yield stress at 650 °C, further plasticity was achieved in the first temperature cycle (i.e. heating from 450 to 650 °C). Beyond that point, the evolution of strain was gradual and proportional to the number of temperature/creep cycles (ratcheting creep). We note that obvious surface changes (due to high levels of plastic strains and paint delamination) were observed beyond cycle 399. These surface changes prohibited further measurements of full-field strains using DIC. The experiment however was not interrupted until sample failure.

Under such thermo-mechanical fatigue loading conditions, the total measured strains contain both thermal and mechanical



17 Contour plot of the effective plastic strain field (ϵ_{eff}) for selected regions showing examples of transmission and shielding. The length of the localised slip bands varies (see for example L_{S1} and L_{S2}). *b* SEM image of the same region after crack formation. The lengths of the microcracks (L_{C1} and L_{C2}) correlate with the measured lengths of the strain localisation bands in *a*. *c* Histogram of L_S across the entire region of interest. *d* Histogram of L_C which was measured 9,000 cycles after strain measurements. Adapted from Figures 9 and 10 in ⁵².

20 components. The evolution of the ϵ_{yy} strain at the beginning and end of each temperature cycle is shown in Figure 22 (i.e. net strain at 450 °C, which is represented with black triangles in Figure 22, and 650 °C which is represented with red squares). The difference between these two points represents predominately the thermal strain due to thermal expansion. The mechanical strain includes the elastic, plastic, and creep components. As the load was held constant during the experiment, the accumulation of strains once temperature cycling was started is creep dominated (i.e. mechanical strain).

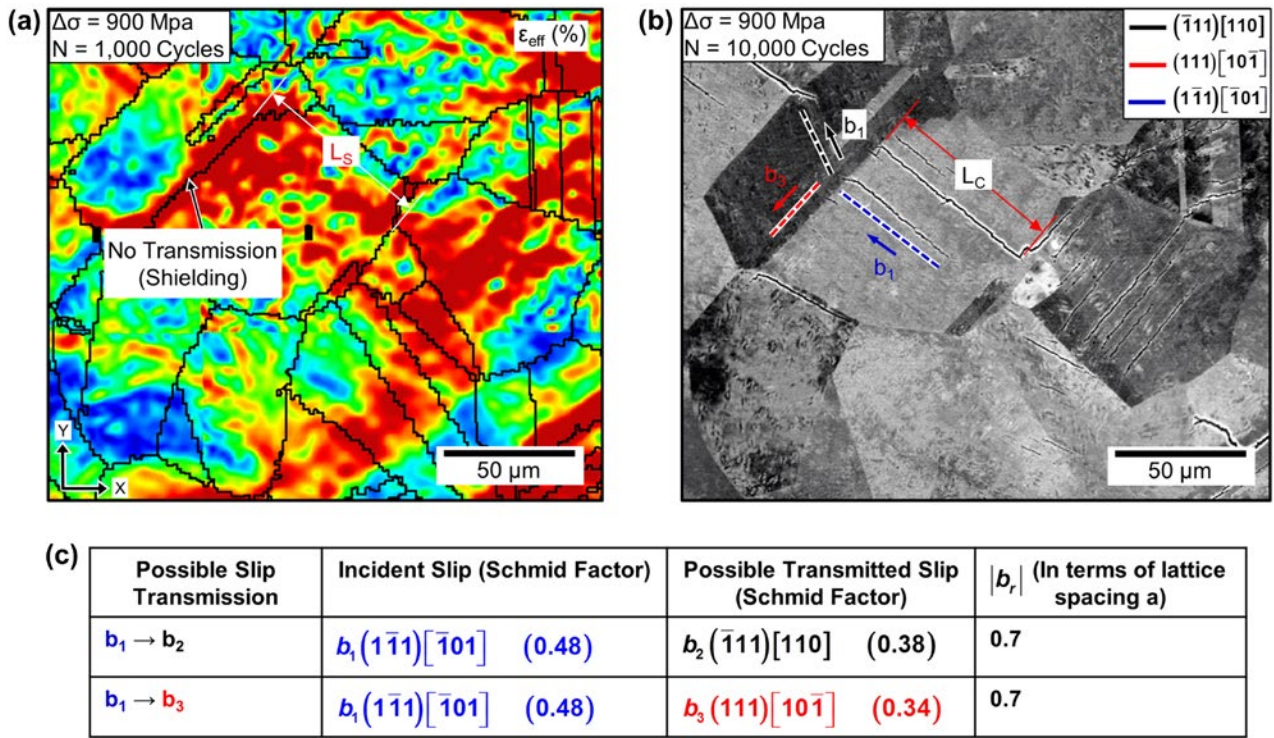
25 Figure 23 shows contour plots of the ϵ_{yy} vertical strain (along the loading direction) for three selected cycles are shown. The contour level scale for each plot was increased to elucidate the fact that the creep dominated mechanical strain accumulated in the same regions (notice the similarity in the contour plot features). Strain histograms were also constructed from the DIC strain measurements. Selected cases are shown in Figure 24 for the strains after 19, 99, 199, and 299 temperature cycles. Both of the plots shown in Figures 23 and 24 provide evidence of an increased level of deformation heterogeneity that was induced in the material by the continuous accumulation of creep strains (seen by the widening of the strain histograms with increase in cycle number). To put the previous data in terms of strain rate, the evolution of the mean, minimum, and maximum strains in the DIC region of interest was plotted as shown in Figure 25. The corresponding strain rates were calculated from the curves in Figure 25 and are reported in Table 1.

The results show significant variation between the three strain rates and clearly demonstrate how the consideration of only the mean strain rate, which is the only measurement available from conventional techniques (i.e. extensometer) and predominantly used in modelling work, underestimates the level of strain build-up in the high strain regions.

30 The observations that the degree of heterogeneity increases and strain predominantly accumulated, spatially, in the same regions on the sample's surface suggest that the local microstructure has a dominant affect in defining the critical regions or hot spots of high strains. We note that higher resolution DIC measurements along with EBSD characterisation would be interesting to obtain in similar thermo-mechanical loading conditions and could provide further insight into the role played by GBs in shaping the strain map and dictating where creep strains will accumulate. However, the tools required for making these measurements have not been fully developed yet.

Discussion

35 The focus of this work has been on deformation in the vicinity of GBs. With the use of full-field measurements of strain and grain orientation with sub-grain level resolution, we quantify the residual plastic strains, the activated slip systems, and the GB type for each of the GBs in the region of interest. The measured heterogeneity in the residual plastic strains was clearly associated with particular regions accommodating the



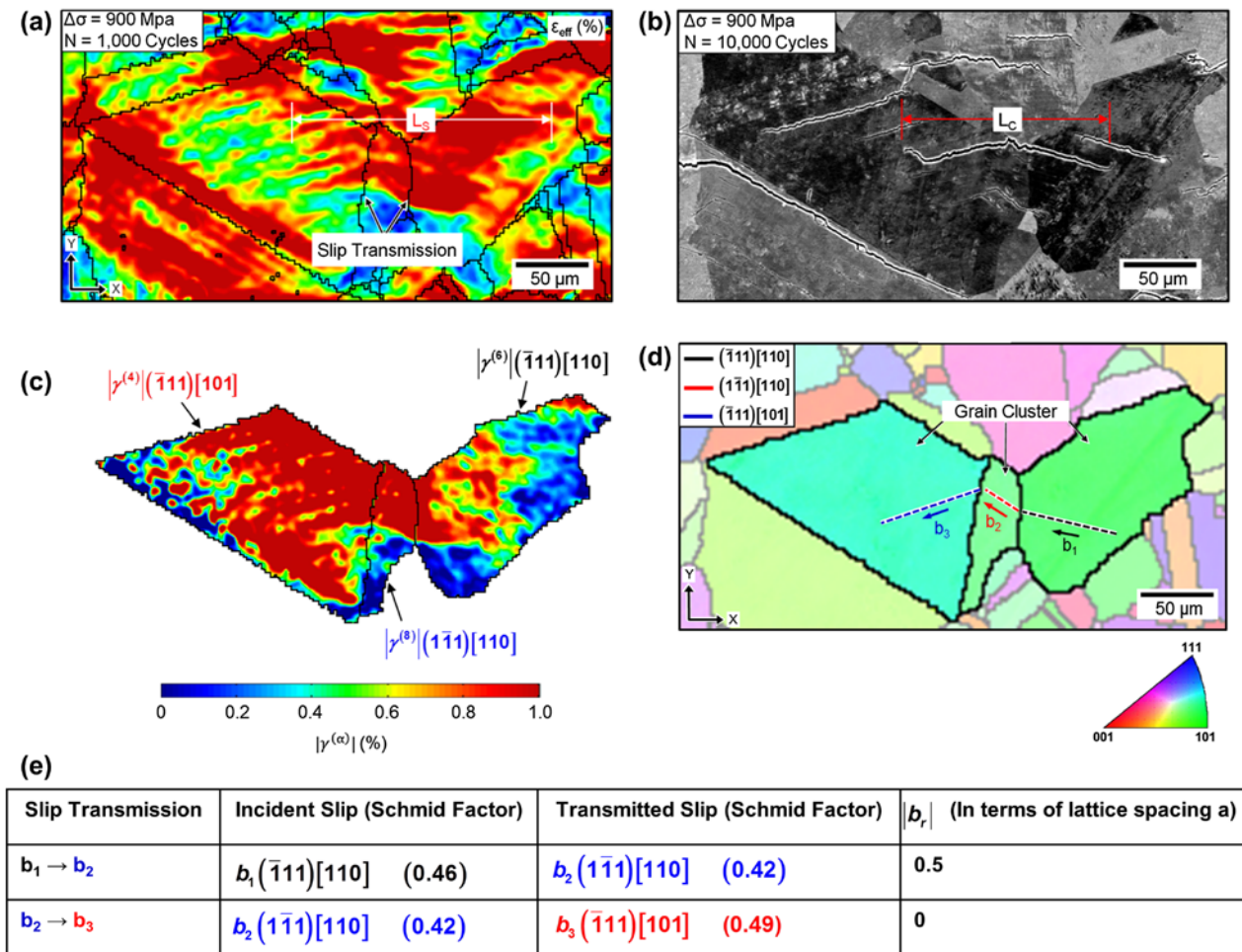
18 a Contour plot of (ϵ_{eff}^p) for a selected region showing an example of shielding at a GB. b SEM image after crack formation. Notice the similarity between crack length L_c and slip band length L_s . Micro-cracks were confined within the grain which exhibited pronounced slip activity, as shown in a, and did not extend across the shielding GB. In the SEM image, b_1 (blue trace) represents the activated slip system of the incident slip and b_2 (black trace) and b_3 (red trace) are the traces of the two slip systems with the highest Schmid factors across the GB. The reactions associated with activation of any of these two systems through transmission from b_1 are reported in c. Notice the high magnitudes of b_r which may have contributed to fact that transmission did not occur. Adapted from Figure 14 in ⁵².

20 majority of the plastic strains while other regions remained
 at relatively low or even zero strain. As GB information
 was available from EBSD, we highlighted that this clear
 selectivity in where strains accumulated was influenced by the
 microstructure. Particularly, some GB regions showed very
 25 high strains across the interface, while others acted as a shield
 with high strains on one side of the GB only. Other researchers
 have made similar observations from experimental work⁵⁵
 and crystal plasticity simulations.⁵⁶ We, however, associate
 these two different GB responses, in terms of dissimilar
 strain accumulation across GBs, with slip transmission (high
 30 strains across the interface) and shielding (high strains on
 one side of the GB, note that this manifestation of the GB
 acting as an obstacle to slip propagation formed the basis
 for generalisation of the Hall-Petch relation⁹). The SEM
 35 micrographs of GB regions associated with slip transmission
 (based on measurements of high strains on both sides of the
 GB) provide clear images of continuous slip traces across
 the interface. This provides some evidence on the validity
 of the assumption that slip transmission must have occurred.
 However, there is the obvious possibility of other reactions
 taking place (e.g. slip nucleation at the GB) leading to the
 40 final outcome that we observe. TEM and *in situ* TEM can
 provide more detailed analysis of the reactions taking place
 at the GB, but covering the entire region of interest with such
 analysis would not be practical.

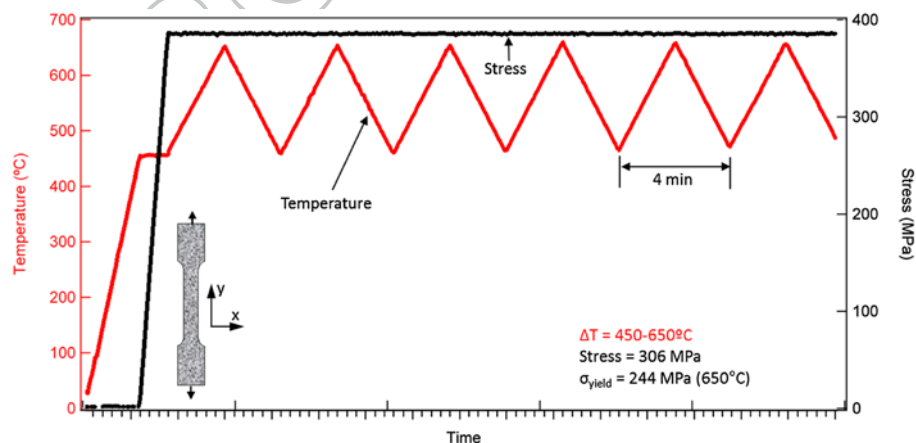
45 In the analysis of slip transmission, we have primarily
 considered the magnitude of b_r and to some extent the
 Schmid factor. Although this particular aspect has been
 extensively studied in the literature as to how it influences
 the transmitted slip system across the GB, we approach the

subject from a different perspective and study if there is an
 impact on the accumulation of strains across both sides of
 50 a transmitting GB. By interrogating hundreds of GBs
 across the entire region of interest, we show examples
 that do not favour slip transmission across the GB when
 high b_r will result (Figure 8) and examples where slip
 extends across the GB and the analysis shows a low
 55 magnitude of b_r . For statistical assessment, this type of
 analysis was extended across hundreds of GBs in the
 region of interest and an inverse relation between strain
 accumulation across interfaces and the magnitudes of
 b_r was shown. This highlights that the reactions taking
 place at GBs are very important in describing the local
 60 material response (not only individual grain orientation
 is important), dictating to some extent the regions
 where strain accumulates (particularly in the vicinity
 of GBs), controlling the formation of grain clusters, and
 5 impacting the formation of fatigue cracks. These aspects
 have also been emphasised and discussed in details in
 the following recent reviews.^{27,28}

In the detailed analysis of the incremental
 monotonic loading case, a clear evolution of plastic
 strain heterogeneity was measured. The sustained
 10 accumulation of strain in the same spatial region (i.e.
 grain clusters connected with transmitting GBs) and
 the lack of activity in other regions was the key factor
 leading to such an increase in heterogeneity. The result
 5 is particularly important if considered from a fatigue
 perspective. As localised plastic slip is a precursor to
 fatigue crack initiation, and as the incremental loading
 results show that the hot spots or locations for localised



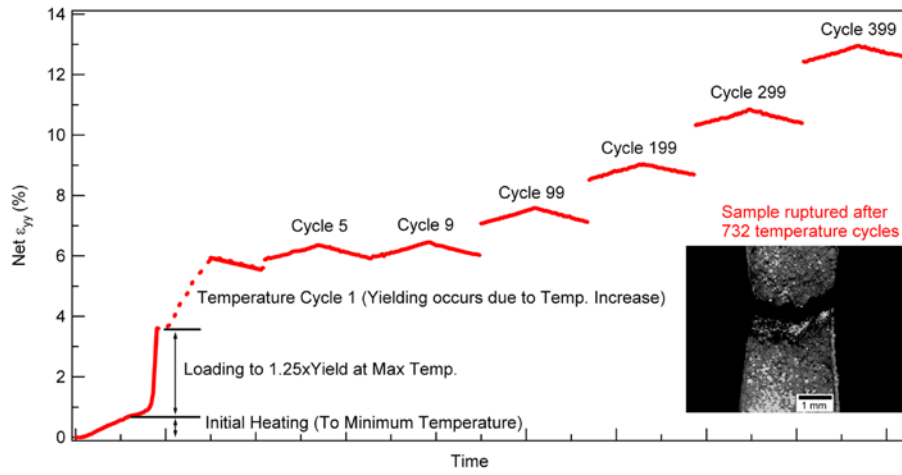
19 a Contour plot of the effective plastic strain field (ϵ_{eff}^p) for a selected region showing an example of slip transmission across the GB. b SEM image of the same region after crack formation. c Contour plots of the shear strains for the incident and transmitted slips across the GBs shown in a. Traces of the activated slip planes are shown on the EBSD grain orientation map in d. The slip transmission reactions are shown in e. Notice that the transmitted system through the first GB acts as incident slip for the other GB to left of the figure. This sequence of slip transmission through multiple GBs leads to the formation of a grain cluster and a long band of strain localisation. Adapted from Figures 15 and 16 in ⁵².



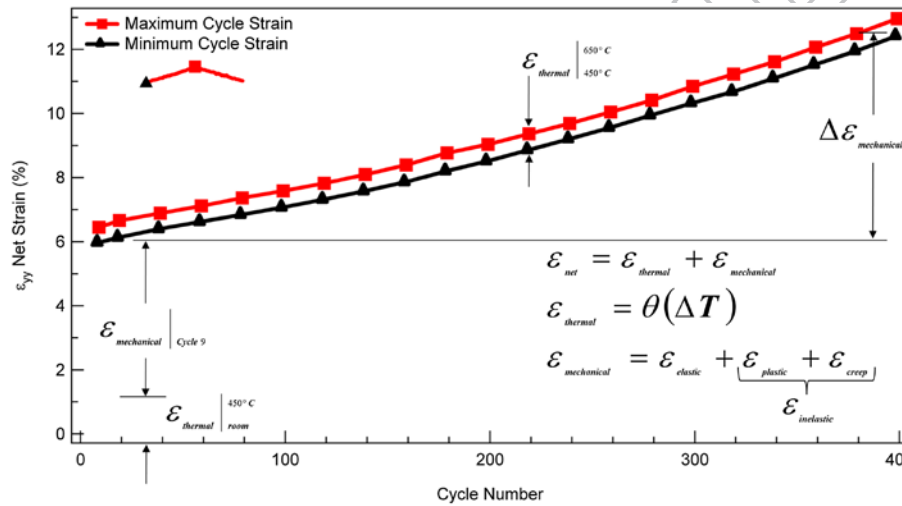
20 Loading conditions for the cyclic creep experiment. The temperature was initially increased from room temperature to 450 °C and then the load on the sample was increased to a final stress level of 306 MPa. Once that point was reached, the load was held constant throughout the test and the temperature was cycled between 450 and 650 °C.

plasticity are formed early and at low levels of strain, the probable sites for crack initiation can, therefore, potentially be predicted. This provides support to the approach we followed in the fatigue crack formation experimental work.

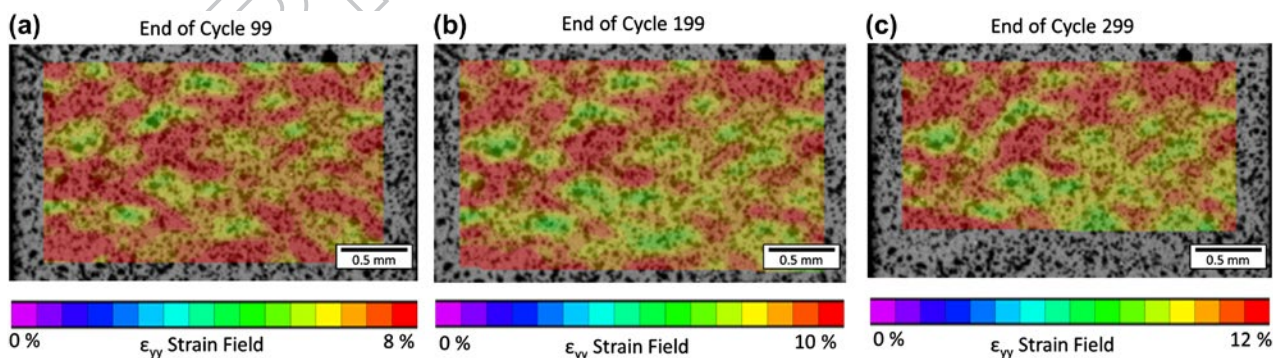
The experimental results under fatigue loading provide a quantitative assessment of the correlation between the location and length of fatigue cracks and prior strain localisations at the grain level. This notion that local plasticity is a precursor to the initiation of fatigue cracks is well known,



21 Strain evolution (DIC field averages) for selected cycles. Notice that yielding takes place once the load on the sample was initially increased from 0 to 306 MPa. Additional accumulation of plastic strains was also measured in the first temperature cycle (i.e. heating from 450 to 650 °C) due to changes in material properties. The evolution of strains beyond that point was gradual and a function of cycle number. DIC measurements beyond cycle 399 were not possible due to significant damage to the surface.



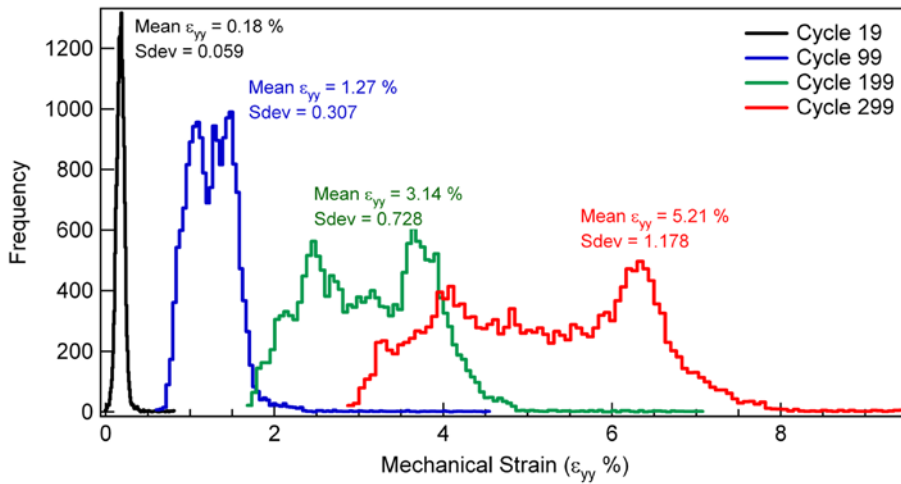
22 The evolution of the minimum cycle strain (black triangles representing the DIC field averages at 450 °C) and maximum cycle strain (red squares representing the DIC field averages at 650 °C).



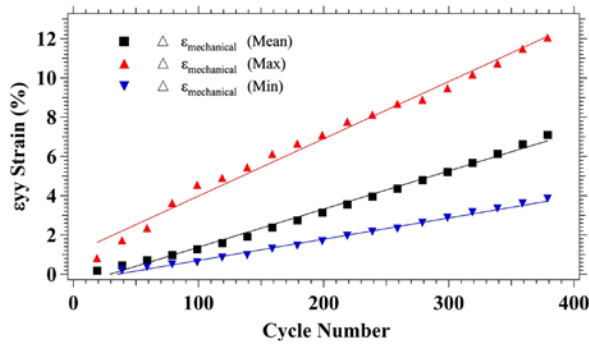
23 Contour plots of the vertical strain fields (along the loading direction) after certain number of temperature cycles (three representative cases). The results clearly show strain accumulation in the same regions.

15 but clear experimental evidence establishing this one-to-one connection, not only in terms of location but also in terms of the length or severity of the formed cracks, is an outcome of this work. One possible benefit of the results is that they

can help fatigue modelling work (primarily the meso-scale models or crystal plasticity models where microstructure is considered) locate the hot spots for crack initiation (high strain region) and pinpoint the most probable locations that



24 Strain histograms after certain number of temperature cycles. The increase in the width of the histograms with additional temperature cycles points to an increased level of deformation heterogeneity developing in the material. This is also observed by noticing the increase in the standard deviation (given in the figure for each histogram).



25 Mechanical strain evolution vs. cycle number (temperature cycle). Black points are from average DIC fields, red and blue points are from low and high strain regions, respectively, as observed in the full-field strain contour plots. Notice that the rate of evolution for the high and low strains is different than the mean strain.

Table 1 Mean, minimum, and maximum creep strain rates.

Strain	$\dot{\epsilon}$ (%/Cycle)	$\dot{\epsilon}$ (%/hour)
ϵ_{yy} Mean DIC strain	0.019	0.292
ϵ_{yy} Minimum DIC strain	0.011	0.162
ϵ_{yy} Maximum DIC strain	0.029	0.438

would turn into severe cracks (i.e. the grain clusters having the longest slip band length). Also, at some point, fatigue models need to transition from crack initiation to fatigue crack growth (when the focus is total life and not just initiation life), the length of the localised slip band can potentially be used as an initial crack length in such analysis.

The importance of the reactions taking place in the vicinity of GBs is significant in fatigue.⁵⁷⁻⁵⁹ The most obvious and widely accepted as being the most impactful is the case of a pile-up formed by impinging slip on the GB. The stress concentration formed due to the pile-up leads to the initiation of cracks. The shielding cases discussed here are examples of such reaction. We note, however, that the associated cracks were in general shorter and confined to a single grain

compared to the fatigue cracks across transmitting GBs which extended across multiple grains following the length of the prior strain localisation. Therefore, and for better depiction of the most critical case leading to the longest fatigue cracks, careful assessment and analysis of the GB response are needed. We note that consideration of the maximum strain has been occasionally used in fatigue initiation models in forming initiation criteria (CP-based models primarily). Based on the results of this work, just mapping out the local strain field without consideration of GBs as shielding or transmitting slip will not point to the most critical grain cluster with the longest slip localisation across multiple grains.

We attribute the formation of grain clusters due to GBs allowing slip transmission. In the cases analysed, the measurement of strain across transmitting GBs and the low magnitudes of residual Burgers vector seem to support our interpretation. There are, however, different opinions in the literature addressing the formation of grain clusters. For example, Davidson *et al.*, view a grain cluster as a group of grains connected by low angle grain boundaries forming a ‘supergrain’ that promotes fatigue crack initiation because of its size.¹⁵ The consideration of misorientation alone does not provide sufficient information to describe if a GB will allow or block slip. For example, in some cases, slip transmission can take place across twin boundaries (high angle GBs) by cross slip. Therefore, the consideration of the other important factors, such as the residual Burgers vector, is important when trying to predict the response of slip-GB interaction (shielding or transmitting GB).¹⁴

In the high temperature results, we again observed that creep strain continued to accumulate in the same regions that were activated following the first mechanical loading cycle. This correlation between the location of initial plasticity due to mechanical load and creep strain build-up with temperature cycling suggests that there was no change in the primary deformation mechanism. Dislocation slip is expected to be the main contributing mechanism to the build-up of creep strain (at least in the temperature and load regime considered). We note however, and compared to the monotonic tension case at room temperature, the strain histograms show that the minimum strain did change and increase with the accumulation of creep strain. Such an increase was not

detected in the room temperature uniaxial case (Figure 12). This indicates the activation of slip in new regions that would not have been active at room temperature.

Microstructural changes, such as the formation of precipitates at high temperatures can influence material behaviour. Zhao *et al.*, have constructed the TTT diagram for Hastelloy X,⁶⁰ and based on their results, and considering the maximum temperature in the range used in this work (i.e. 650 °C) and the time for the reported DIC results (i.e. 400 cycles corresponding to about 27 h), it is unlikely that any significant changes in precipitate formation took place (e.g. $M_{23}C_6$ and $M_{12}C$). It will be of interest to consider other loading conditions or heat treatment options creating precipitates to better understand how the presence of precipitates would impact the development of plastic deformation heterogeneity. Also, as some of the precipitates stack at twin or grain boundaries,^{38,60} studying how much their presence will impact slip transmission and strain accumulation across interfaces will help advance our understanding of changes in the local material response due to microstructural changes taking place at elevated temperatures.

Finally, we conclude this discussion with some limitations that are worth pointing out:

- (1) The DIC/EBSD analysis, as any surface measurement technique, provides no information on the bulk of the material and any subsurface effects cannot be quantified. Crystal plasticity simulations may provide insight into subsurface contributions, however, on the experimental side, although X-ray diffraction techniques can be used for 3D orientation mapping,⁶¹ full-field strain measurements through the volume will be challenging and still require significant technique development.
- (2) The high resolution strain measurements discussed in this work are essentially a single snap shot of a deformed state (*ex-situ*). An *in situ* experiment showing the full details of the evolution of strain in time would provide a clearer picture of, for example, where slip initially nucleated and where transmission took place. This will also be useful for the analysis of fatigue crack formation as the exact point in time when the observed cracks formed is unknown in our analysis. *In situ* experimental work will help address this limitation, but more technique development is needed to enable such measurements with adequate resolution.

Conclusions

The work presented in this work supports the following conclusions:

- (1) In all the cases considered in this study, the local microstructure played a major role in inducing deformation heterogeneity. A wide range of strain magnitudes was measured with obvious influence from GBs as either allowing the accumulation of strain across the interface or acting as shields in which slip was prevented from propagating across the GB leading to the build-up of strain in certain regions and the lack of slip activity in others.
- (2) The high-resolution strain measurements in GB regions allow the demarcation of GBs as transmitting GBs (high strains on both side of the GB) or shielding GBs (high strains on one side only). SEM micrographs showing continuity of slip traces across transmitting GBs (as depicted based on strain accumulation

across the interface) provide support to the approach we followed in describing the possible reaction taking place at the GB based on high resolution strain measurements.

- (3) The residual Burgers vector b_r is shown to be very influential in dictating the cross-boundary reaction and affecting the magnitude of strain accumulation across interfaces. These observations and conclusions were based on strain and grain orientation measurements to determine the local slip system activity of GBs and b_r . A major advantage in the approach followed in this work is the ability to investigate hundreds of GBs and thus provide statistical assessment of the importance of b_r in affecting the local deformation heterogeneity in a plastically deforming metal. A clear positive correlation between the magnitudes of strains across GBs and the magnitude of b_r was observed in this work.
- (4) For the various loading conditions considered in this work (i.e. monotonic tension, fatigue, and cyclic creep), the majority of slip activity and the accumulation of plastic strain were confined in specific regions. We observed signs of early formation of grain clusters (i.e. strain accumulation in regions connected by transmitting GBs). Continued loading resulted in sustained build-up of strain in the same regions and thus resulting in an increased level of deformation heterogeneity with continued loading.
- (5) The fatigue micro-crack formation results show a clear correlation between regions of localised plasticity, early in the life of the sample, and the eventual formation of fatigue micro-cracks. This correlation was shown to be in both location and severity of cracks; regions with longer slip bands of localised slip resulted in more severe cracks following the length of these bands.
- (6) The severity of fatigue micro-cracks was shown to be influenced by the reactions taking place at the GB. In GBs allowing slip transmission, slip bands extended across multiple grains leading to the formation of larger grain clusters. Fatigue cracks in this case were shown to extend across the grain cluster following the length of the slip band through all the involved. On the other hand, shielding GBs resulted in isolated slip bands that are shorter and confined in single grains. The resulting fatigue micro-cracks were shorter in this case.
- (7) The full-field analysis of strain evolution under cyclic creep conditions has enabled us to assess the local variation in creep strain rate. The results show significant variation between the minimum, mean, and maximum strains rates (in the DIC field) and clearly demonstrate how the consideration of only the mean strain rate underestimates the level of strain build-up in the high strain regions.

Funding

This work was funded by the Midwest Structural Sciences Center (MSSC); Air Vehicles Directorate of the U.S. Air Force Research Laboratory [grant number FA8650-06-2-3620]; EBSD results were obtained at the Frederick Seitz Materials Research Laboratory Central Facilities, University of Illinois, which are partially supported by the U.S. Department of Energy [grant number DE-FG02-07ER46453], [grant number DE-FG02-07ER46471].

References

- 25 1. J. Gemperlová, V. Paidar and F. Kroupa: *Czechoslovak J. Phys.*, 1989, **39**, (4), 427.
- AQ7 2. J. P. Hirth: *Metall. Trans.*, 1972, **3**, (12), 3047.
3. J. Miao, T. M. Pollock and J. Wayne Jones: *Acta Mater.*, 2009, **57**, (20), 5964.
- 30 4. P. Peralta, L. Llanes, J. Bassani and C. Laird: *Philos. Mag. A*, 1994, **70**, (1), 219.
5. A. P. Sutton and R. W. Balluffi: 'Interfaces in crystalline materials'; 2006, Oxford, Oxford Classical Texts.
- 35 6. J. D. Eshelby, F. C. Frank and F. R. N. Nabarro: *Philos. Mag.*, 1951, **42**, 351–364.
7. E. O. Hall: *Proc. Phys. Soc. London*, 1951, **64**, 747–753.
8. N. J. Petch: *J. Iron Steel Inst.*, 1953, **174**, 25–28.
9. R. Armstrong, I. Codd, R. M. Douthwaite and N. J. Petch: *Philos. Mag.*, 1962, **7**, (73), 45.
- 40 10. T. C. Lee, I. M. Robertson and H. K. Birnbaum: *Metall. Trans. A*, 1990, **21**, (9), 2437.
11. L. C. Lim and R. Raj: *Acta Metall.*, 1985, **33**, (8), 1577.
12. J. D. Livingston and B. Chalmers: *Acta Metall.*, 1957, **5**, (6), 322.
- AQ8 13. A. Pineau: *Philos. Trans. R. Soc. London A: Math. Phys. Eng. Sci.*, 2015, **373**, (2038).
- 45 14. W. Abuzaid, M. D. Sangid, J. D. Carroll, H. Sehitoglu and J. Lambros: *J. Mech. Phys. Solids*, 2012, **60**, (6), 1201–1220.
15. D. Davidson, R. Tryon, M. Oja, R. Matthews and K. Ravi Chandran: *Metall. Mater. Trans. A*, 2007, **38**, (13), 2214.
16. Y. Guilhem, S. Basseville, F. Curtit, J. M. Stéphan and G. Cailletaud: *Int. J. Fatigue*, 2010, **32**, (11), 1748.
- 50 17. M. D. Sangid, H. J. Maier and H. Sehitoglu: *J. Mech. Phys. Solids*, 2011, **59**, (3), 595.
18. T. C. Lee, I. M. Robertson and H. K. Birnbaum: *Scr. Metall.*, 1989, **23**, (5), 799.
19. L. C. Lim: *Scr. Metall.*, 1984, **18**, (10), 1139.
- 55 20. D. E. Spearot and M. D. Sangid: *Curr. Opin. Solid State Mater. Sci.*, 2014, **18**, (4), 188.
21. M. Dewald and W. A. Curtin: *Modell. Simul. Mater. Sci. Eng.*, 2011, **19**, (5).
22. Z. H. Jin, P. Gumbsch, K. Albe, E. Ma, K. Lu, H. Gleiter and H. Hahn: *Acta Mater.*, 2008, **56**, (5), 1126.
- 60 23. M. P. Dewald and W. A. Curtin: *Philos. Mag.*, 2007, **87**, (30), 4615.
24. M. P. Dewald and W. A. Curtin: *Modell. Simul. Mater. Sci. Eng.*, 2007, **15**, (1), S193.
25. F. P. E. Dunne: *Curr. Opin. Solid State Mater. Sci.*, 2014, **18**, (4), 170.
26. H. Mughrabi: *Procedia Eng.*, 2010, **2**, (1), 3.
- 65 27. H. Mughrabi: *Philos. Trans. R. Soc. London A Math. Phys. Eng. Sci.*, 2038, **2015**, 373.
28. S. D. Antolovich and R. W. Armstrong: *Prog. Mater. Sci.*, 2014, **59**, 1.
29. S. Suresh: 'Fatigue of Materials'; 1998, Cambridge University Press.
30. J. D. Carroll, W. Abuzaid, J. Lambros and H. Sehitoglu: *Int. J. Fatigue*, 2012.
- 70 31. T. Niendorf, J. Dadda, D. Canadinc, H. J. Maier and I. Karaman: *Mater. Sci. Eng. A*, 2009, **517**, (1–2), 225.
32. E. E. Sackett, L. Germain and M. R. Bache: *Int. J. Fatigue*, 2007, **29**, (9–11), 2015.
33. A. S. Cheng and C. Laird: *Fatigue Fract. Eng. Mater. Struct.*, 1981, **4**, (4), 343.
34. J. M. Finney and C. Laird: *Philos. Mag.*, 1975, **31**, (2), 339.
- 75 35. C. Laird, J. M. Finney and D. Kuhlmann-Wilsdorf: *Mater. Sci. Eng.*, 1981, **50**, (1), 127.
36. H. Mughrabi, R. Wang, K. Differt and U. Essmann: *ASTM*, 1983, 5. AQ9
37. M. A. Rowley and E. A. Thornton: *J. Eng. Mater. Technol.*, 1996, **118**, (1), 19.
38. T. Sakthivel, K. Laha, M. Nandagopal, K. S. Chandravathi, P. Parameswaran, S. Panneer Selvi, M. D. Mathew and S. K. Mannan: *Mater. Sci. Eng. A*, 2012, **534**, 580. 80
39. B. Swaminathan, W. Abuzaid, H. Sehitoglu and J. Lambros: *Int. J. Plast.*, 2015, **64**, 177.
40. M. G. Castelli, R. V. Miner, and D. N. Robinson: 'Thermomechanical deformation behavior of a dynamic strain aging alloy, Hastelloy X', Symposium on Thermomechanical Fatigue Behavior of Materials, San Diego, CA, USA; 1992, American Society for Testing and Materials. 85
41. H. U. Hong, I. S. Kim, B. G. Choi, H. W. Jeong and C. Y. Jo: *Mater. Lett.*, 2008, **62**, (28), 4351.
42. R. L. McDaniels, L. Chen, R. Steward, P. K. Liaw, R. A. Buchanan, S. White, K. Liaw and D. L. Klarstrom: *Mater. Sci. Eng. A*, 2011, **528**, (12), 3952. 90
43. M. C. Casperson, J. D. Carroll, J. Lambros, H. Sehitoglu and R. H. Dodds Jr: *Int. J. Fatigue*, 2014, **61**, 10.
44. W. Hoffelner and P. Gudmundson: *Eng. Fract. Mech.*, 1982, **16**, (3), 365.
45. K. S. Kim and R. H. Van Stone: *Eng. Fract. Mech.*, 1997, **58**, (1–2), 133. 95
46. K. Krompholz, E. D. Grosser and K. Ewert: *Materialwissenschaft und Werkstofftechnik*, 1982, **13**, (7), 236.
47. Y. L. Lu, P. K. Liaw, L. J. Chen, G. Y. Wang, M. L. Benson, S. A. Thompson, J. W. Blust, P. F. Browning, A. K. Bhattacharya, J. M. Aurrecoechea and D. L. Klarstrom: *Mat. Sci. Eng. A*, 2006, **433**, (1–2), 114.
48. T. Uga: *Int. J. Press. Vessels Pip.*, 1994, **57**, (3), 305. 100
49. Y. Yoshioka, N. Okabe, D. Saito and K. Fujiyama: *J. Soc. Mat. Sci.*, 1994, **43**, (484), 36–40.
50. S. Abotula, A. Shukla and R. Chona: *J. Mater. Sci.*, 2011, **46**, (14), 4971–4979.
51. T. Sakthivel, K. Laha, M. Nandagopal, K. S. Chandravathi, P. Parameswaran, S. Panneer Selvi, M. D. Mathew and S. K. Mannan: *Mater. Sci. Eng. A*, 2015, **534**, 580. 105
52. W. Abuzaid, H. Sehitoglu and J. Lambros: *Mater. Sci. Eng. A*, 2012, **561**, 507.
53. T. N. Baker and N. J. Petch: 'Yield, flow and fracture of polycrystals'; 1983, Applied Science.
54. U. F. Kocks and H. Chandra: *Acta Metall.*, 1982, **30**, (3), 695. 110
55. M. A. Tschopp, B. B. Bartha, W. J. Porter, P. T. Murray and S. B. Fairchild: *Metall. Mater. Trans. A*, 2009, **40**, (10), 2363.
56. A. D. Rollett, R. A. Lebensohn, M. Groeber, Y. Choi, J. Li and G. S. Rohrer: *Modell. Simul. Mater. Sci. Eng.*, 2010, **18**, (7).
57. T. R. Bieler, P. Eisenlohr, F. Roters, D. Kumar, D. E. Mason, M. A. Crimp and D. Raabe: *Int. J. Plast.*, 2009, **25**, (9), 1655.
58. T. R. Bieler, P. Eisenlohr, C. Zhang, H. J. Phukan and M. A. Crimp: *Curr. Opin. Solid State Mater. Sci.*, 2014, **18**, (4), 212.
59. A. Ma, F. Roters and D. Raabe: *Acta Mater.*, 2006, **54**, (8), 2181.
60. J. C. Zhao, M. Larsen and V. Ravikumar: *Mater. Sci. Eng. A*, 2000, **293**, (1–2), 112.
61. U. Lienert, S. Li, C. Hefferan, J. Lind, R. Suter, J. Bernier, N. Barton, M. Brandes, M. Mills, M. Miller, B. Jakobsen and W. Pantleon: *JOM J. Miner. Met. Mater. Soc.*, 2011, **63**, (7), 70.
62. W. Abuzaid, M. D. Sangid, H. Sehitoglu, J. Carroll and J. Lambros: *Procedia IUTAM*, 2012, **4**, 169.